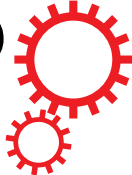


SCIENTIFIC REPORTS



OPEN

Chemical Vapor Deposition of Monolayer $\text{Mo}_{1-x}\text{W}_x\text{S}_2$ Crystals with Tunable Band Gaps

Ziqian Wang¹, Pan Liu², Yoshikazu Ito^{2,3}, Shoucong Ning⁴, Yongwen Tan², Takeshi Fujita^{2,3}, Akihiko Hirata^{2,3} & Mingwei Chen^{1,2,3}

Received: 15 December 2015

Accepted: 27 January 2016

Published: 22 February 2016

Band gap engineering of monolayer transition metal dichalcogenides, such as MoS_2 and WS_2 , is essential for the applications of the two-dimensional (2D) crystals in electronic and optoelectronic devices. Although it is known that chemical mixture can evidently change the band gaps of alloyed $\text{Mo}_{1-x}\text{W}_x\text{S}_2$ crystals, the successful growth of $\text{Mo}_{1-x}\text{W}_x\text{S}_2$ monolayers with tunable Mo/W ratios has not been realized by conventional chemical vapor deposition. Herein, we developed a low-pressure chemical vapor deposition (LP-CVD) method to grow monolayer $\text{Mo}_{1-x}\text{W}_x\text{S}_2$ ($x = 0-1$) 2D crystals with a wide range of Mo/W ratios. Raman spectroscopy and high-resolution transmission electron microscopy demonstrate the homogeneous mixture of Mo and W in the 2D alloys. Photoluminescence measurements show that the optical band gaps of the monolayer $\text{Mo}_{1-x}\text{W}_x\text{S}_2$ crystals strongly depend on the Mo/W ratios and continuously tunable band gap can be achieved by controlling the W or Mo portion by the LP-CVD.

Band gap engineering is indispensable in nowadays electronics and optoelectronics since a variety of artificial band gaps build on the basics for the optimization and innovation in diverse device applications. Recently, the emergence of two dimensional (2D) materials with a direct band gap opens up a new avenue for improving the integrity in devices. Similar to the bulk semiconductors, the band gaps of 2D materials are changeable and can be modified by applying strains¹⁻⁵, functionalization^{6,7} and chemical doping⁸⁻¹⁷. As a promising 2D alloy system, the direct band gaps of monolayer $\text{Mo}_{1-x}\text{W}_x\text{S}_2$ crystals have been demonstrated to strongly depend on Mo/W ratios^{12,15,18}. Although monolayer $\text{Mo}_{1-x}\text{W}_x\text{S}_2$ nanosheets have been obtained by mechanical exfoliation^{15,19}, it is technically inappropriate to implement the nano-sized fragments into devices for practical applications. On the other hand, while chemical vapor deposition (CVD) has been widely used to grow monolayer MoS_2 and WS_2 with high crystallinity²⁰⁻³⁶, the atomic-scale uniformly mixed $\text{Mo}_{1-x}\text{W}_x\text{S}_2$ 2D alloys have not been successfully achieved by conventional CVD despite many efforts have been devoted to this problem³⁷⁻³⁹. In previous CVD growth of pristine MoS_2 and WS_2 monolayers, MoO_3 and WO_3 powders have been used as the transition metal sources and S powder as the reductant source^{20-26,28,29,31-34,36}. MoO_3 is partially reduced by sulfur vapor to form volatile MoO_{3-x} at $\sim 500^\circ\text{C}$, and the growth of MoS_2 can be attained at a temperature as low as 530°C ^{21,24}. In contrast, WO_3 or WO_{3-x} has a poor volatility and requires a high temperature up to $\sim 1000^\circ\text{C}$ for vaporization. Thus, the CVD temperature for WS_2 growth is not lower than 800°C by using WO_3 or WO_{3-x} as the precursor^{26,28,33}. The large CVD temperature gap between MoS_2 and WS_2 growth makes it difficult to control the supply of the two oxide precursors for the synthesis of monolayer $\text{Mo}_{1-x}\text{W}_x\text{S}_2$ alloys. As a result, MoS_2 is usually deposited prior to WS_2 , resulting in the formation of two-phase MoS_2/WS_2 heterostructures, rather than $\text{Mo}_{1-x}\text{W}_x\text{S}_2$ alloys with a uniform composition and a well-defined band gap¹⁷. Although very recently monolayer and multi-layer $\text{Mo}_{1-x}\text{W}_x\text{S}_2$ alloys have been obtained by atomic layer deposition¹², sulfurization of co-sputtered $\text{Mo}_{1-x}\text{W}_x$ thin films³⁷ and other methods^{38,39}, the monolithic $\text{Mo}_{1-x}\text{W}_x\text{S}_2$ monolayers with tunable compositions and band gaps have not been realized by the conventional CVD method. In this study, we report a facile method for the synthesis of compositionally homogeneous monolayer $\text{Mo}_{1-x}\text{W}_x\text{S}_2$ ($x = 0-1$) single crystals based on low-pressure (LP) CVD in a conventional CVD system. The band gaps of the synthesized monolayer alloys can be tailored by changing the

¹Department of Materials Science, Graduate School of Engineering, Tohoku University, Sendai 980-8577, Japan.

²WPI Advanced Institute for Materials Research, Tohoku University, Sendai 980-8577, Japan. ³CREST, JST, 4-1-8 Honcho Kawaguchi, Saitama 332-0012, Japan. ⁴Department of Mechanical and Aerospace Engineering, School of Engineering, Hong Kong University of Science and Technology, Clear Water Bay, Kowloon, Hong Kong SAR. Correspondence and requests for materials should be addressed to M.C. (email: mwchen@wpi-aimr.tohoku.ac.jp)

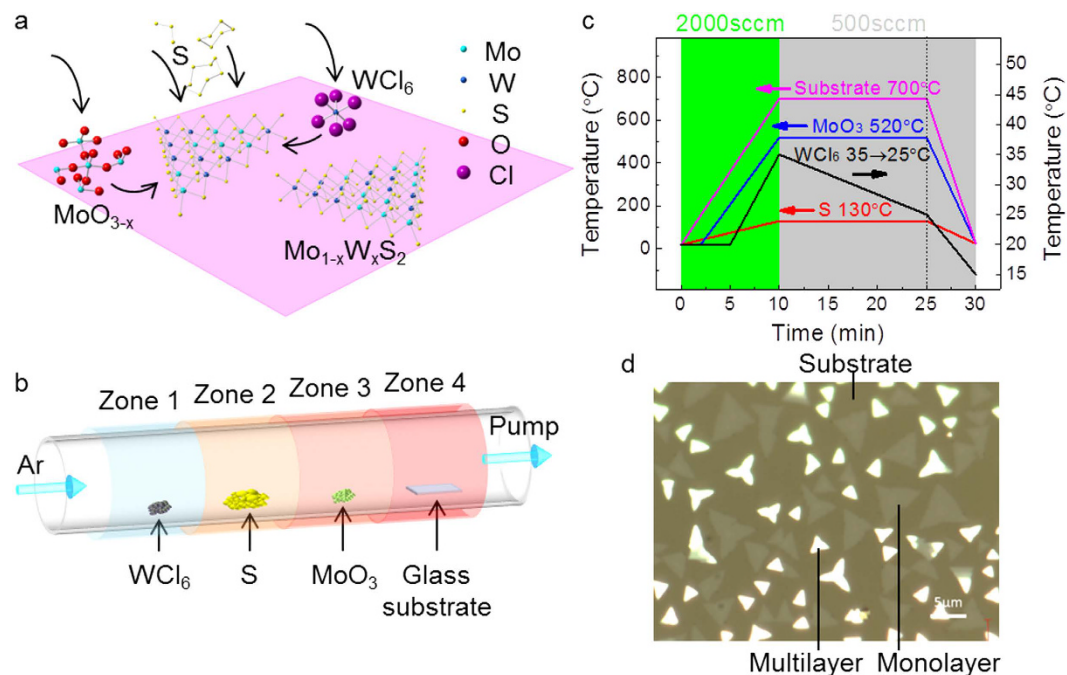


Figure 1. LP-CVD synthesis of monolayer $\text{Mo}_{1-x}\text{W}_x\text{S}_2$ on glass substrates. (a) Schematic illustration of the surface reactions during CVD growth. (b) The arrangement of WCl_6 , sulfur, MoO_3 and substrate in the CVD system. They were placed from upstream to downstream in four different furnace zones. The temperatures of each zone can be controlled independently. (c) Temperature profiles of the precursors and the substrate during CVD growth. The temperatures of each precursor and the substrate rose to their designed values within 10 min under 2000 sccm Ar flow rate. Then, the Ar flow was switched to 500 sccm for film growth. The temperature of the substrate, MoO_3 and S sources were kept constant while the temperature of WCl_6 gradually dropped from 35 to 25 °C in 15 min before cooling down. (d) Optical image showing the triangular flakes grew on the glass substrate (dark regions). Brighter ones are the multilayers and less bright ones are monolayers.

Mo/W ratios, demonstrating the feasibility of realizing band gap engineering in 2D materials by the conventional CVD method.

Results

LP-CVD growth of monolayer $\text{Mo}_{1-x}\text{W}_x\text{S}_2$ alloys. Different from previous CVD studies in which WO_3 powders were used as the W source, in this study a highly volatile W-containing precursor WCl_6 was chosen. WCl_6 sublimates at much lower temperature below 100 °C^{27,30,40} and the temperature required for WS_2 growth can be reduced to ~700 °C, which is very close to the CVD temperature of MoS_2 using MoO_3 as the precursor³⁰. Therefore, MoO_3 and WCl_6 powders can be simultaneously used as the Mo and W sources for the CVD growth of monolayer $\text{Mo}_{1-x}\text{W}_x\text{S}_2$ alloys and the Mo/W ratio can be tailored by tuning the MoO_3 and WCl_6 supplies. Figure 1a schematically illustrates the reactions during CVD process. Gas species MoO_{3-x} and WCl_6 are transported to the glass substrate, adsorb to and diffuse on the surface before being completely sulfurized and rearranged to form a $\text{Mo}_{1-x}\text{W}_x\text{S}_2$ alloy layer. Details about the CVD setup (Fig. 1b) and temperature profile (Fig. 1c) used in this study will be described in Methods section.

We noticed that the formation of MoS_2/WS_2 heterostructures cannot be completely avoided even if the WS_2 growth temperature has been reduced to close to that of MoS_2 by using the highly volatile WCl_6 precursor. This is caused by uncontrollable sublimation of WCl_6 and MoO_3 during CVD temperature rising and cooling. The different temperature dependence of WCl_6 and MoO_3 sublimations leads to the separated deposition of MoS_2 and WS_2 in temperature rising/decreasing stages. To achieve homogeneous growth of monolithic $\text{Mo}_{1-x}\text{W}_x\text{S}_2$ monolayers, the suppression of uncontrollable film deposition during temperature rising and cooling is critical. We utilized a high Ar flow rate to prevent the separate chemical deposition of MoS_2 or WS_2 during CVD temperature rising. It was found that the film deposition can be completely suppressed when the Ar flow rate is higher than ~2000 sccm (Fig. S1a,b, Supplementary Information). This suppression of deposition may originate from the low sublimation rates of sulfur source and MoO_{3-x} and WCl_6 precursors at high pressures at which neither MoS_2 nor WS_2 can grow (Fig. S2, Supplementary Information). After the CVD temperature reaches to the designed value and is stabilized for 1 ~ 2 min, the Ar flow was then decreased to 500 sccm for homogeneous $\text{Mo}_{1-x}\text{W}_x\text{S}_2$ growth.

It has been found that MoO_3 suffers from the reduction by sulfur vapor and only partially reduced volatile MoO_{3-x} can be transported to substrates for $\text{Mo}_{1-x}\text{W}_x\text{S}_2$ growth while nonvolatile MoS_2 by excessive reduction forms a cap layer covering MoO_3 source. The cap layer becomes thicker and thicker with CVD time. Since the production and transport of MoO_{3-x} require sulfur vapor and MoO_{3-x} vapor to diffuse through the MoS_2 cap layer, the nonvolatile MoS_2 cap layer results in the decrease of the MoO_{3-x} supply rate during CVD. In contrast,

the simple sublimation of WCl_6 keeps a constant supply rate at a designed CVD temperature. The de-coupling between the W and Mo supply rates leads to a compositional gradient in the grown monolayer $Mo_{1-x}W_xS_2$ crystals with Mo-rich centers and W-rich rims (Fig. S3, Supplementary Information). Thus, to avoid the composition gradient, it is essential to maintain a constant ratio of Mo and W supply rates, which has been succeeded by gradually lowering down the heating temperature of WCl_6 source during CVD growth as shown in Fig. 1c. Additionally, monolayer $Mo_{1-x}W_xS_2$ samples with different compositions can be obtained by adjusting the amount of the WCl_6 source.

Microstructure characterization of $Mo_{1-x}W_xS_2$ alloys. The LP-CVD method allows us to grow large-scale $Mo_{1-x}W_xS_2$ films with tunable compositions and thickness. However, the continuous 2D films are difficult to be identified by optical microscopy and even scanning electron microscopy (SEM) (Fig. S9). In contrast, the as-grown $Mo_{1-x}W_xS_2$ flakes are visible under an optical microscope (Fig. 1d), which are mainly used for the characterization of structure, chemistry and optical properties. The grey triangular flakes with the lateral size of around $5\ \mu\text{m}$ are monolayer $Mo_{1-x}W_xS_2$ and the bright ones with the size of $2\sim 3\ \mu\text{m}$ are multilayer ones, which can be elucidated by photoluminescence spectroscopy and high-angle annular dark field scanning transmission electron microscopy (HAADF-STEM) images (Fig. S4, Supplementary Information). The as-grown $Mo_{1-x}W_xS_2$ flakes were transferred to holey carbon coated Cu grids for STEM characterization. As shown in Fig. 2a–d, the energy dispersive X-ray spectroscopy (EDS) mappings reveal the homogeneous distributions of Mo, W and S in a triangular flake, manifesting that the as-grown $Mo_{1-x}W_xS_2$ crystals are a homogeneously mixed alloy, rather than a MoS_2/WS_2 heterostructure.

The atomic structure of the monolayer $Mo_{1-x}W_xS_2$ alloys was visualized by HAADF-STEM (Fig. 2e) in which W atoms show a brighter contrast than Mo atoms because of the mass difference. Again, the random mixture of Mo and W atoms in the alloy is confirmed although the short-range chemical order and chemical fluctuation of both W and Mo can be identified in the atomic image. By simply counting the numbers of Mo and W, the compositions of the monolayer samples can be determined. For example, the composition of the sample shown in Fig. 2e is measured to be $Mo_{0.33}W_{0.67}S_2$, which is consistent with the macroscopic composition of $Mo_{0.33}W_{0.67}S_2$ determined by X-ray photoelectron spectroscopy (XPS) from the entire sample. The atomic images reveal that the as-grown $Mo_{1-x}W_xS_2$ monolayer alloys contain two phases: metallic 1T and semiconductor 1H. Although the 1T phase has been observed in pristine MoS_2 and WS_2 before^{41–51}, it is the first observation of 1T in the monolayer $Mo_{1-x}W_xS_2$ grown by CVD. The phase identification is based on the contrast of S atoms. Since S atoms are much lighter than Mo and W, they are almost invisible in the metallic 1T phase due to the misaligned two sulfur layers as shown in Fig. 2e (upper part). In contrast, they are able to show the discriminable contrast in 1H in which two sulfur atomic layers project on each other in each sulfur atomic column and have enhanced intensity in the HAADF-STEM image (Fig. 2e, lower part). Hence, the difference between the atomic structure of 1H and 1T can be easily identified from the intensity profiles taken from the two phases (Fig. 2h). The interface between 1H and 1T phases is indicated by a blue dashed line in Fig. 2e. The intensity profile along the orange dashed line across the phase boundary is shown in Fig. 2i for detailed view. The phase boundary is formed by the displacement of one of the two S layers on a single side in agreement with previous observations in 1T/1H mixed monolayer MoS_2 ^{41,45,49}. The arrangement and orientation of Mo and W atoms remain undisturbed across the 1H/1T interface as confirmed by the nearly identical fast Fourier transform (FFT) patterns (Fig. 2e–g) from two phases (red short dashed line in 1H and green short dashed line in 1T region), similar to previous observations of the co-existence of 1T and 1H in monolayer MoS_2 ⁴¹. Only 1T structure, rather than the distorted 1T (1T') structure which is often observed in 1T- WS_2 monolayer^{47,52}, was observed even at locally W-rich compositions ($x = 0.6\sim 0.8$). In addition, the domain sizes of the 1T phase appear larger than tens of nanometers since a single domain cannot be covered by the field of vision in STEM at a magnification large enough for the discrimination of 1T or 1H phase. The relation between the local Mo/W atomic ratio and 1T or 1H phase in the $Mo_{0.33}W_{0.67}S_2$ 2D crystals is statistically analyzed by using the HAADF-STEM images randomly acquired from different regions of 1T and 1H phases. Both phases have a similar and homogeneous composition with small variation of local W proportion in the range from $\sim 60\%$ to $\sim 80\%$. Based on a typical HAADF-STEM image, spatial distribution of W proportion x is shown in Fig. S5a,b (Supplementary Information), revealing a small compositional fluctuation of $x = 0.58\sim 0.78$ in nanometer scale. Both the distribution of nearest Mo neighbors of Mo and Mo neighbors of W show similar Gaussian distribution centered near the macroscopic value (2.0 for $x = 0.67$) (Fig. S5c,d, Supplementary Information). The standard deviation of the average number of the nearest Mo neighbors of Mo and W atoms from $6(1-x)$ ($x = 0.67$ in this case) are 1.19 and 1.14 corresponding to Fig. S5c,d respectively, manifesting the atomic scale homogeneity of the as-grown sample.

X-ray photoelectron spectroscopy (XPS) analysis. XPS was used to study the valence states and chemical composition of the 2D $Mo_{1-x}W_xS_2$ alloys. Figure 3 (upper) shows the XPS results of Mo and W in the as-grown $Mo_{0.33}W_{0.67}S_2$ alloy. For comparison, we also measured the XPS spectra of monolayer MoS_2 (Fig. 3 lower left) and WS_2 (Fig. 3 lower right) grown under the same CVD conditions by using single precursors. Based on the valence states, the trigonal prismatic 1H phase and octahedral 1T phase, can be identified from the XPS spectra^{46–51,53,54}. In contrast to the spectra of pristine MoS_2 and WS_2 monolayers which only show the XPS peaks from the trigonal prismatic 1H phase, the splitting of Mo or W bands in $Mo_{1-x}W_xS_2$ samples verifies the coexistence of 1H and 1T phases, confirming the HAADF-STEM observations. The core levels of Mo $3d_{3/2}$ at 232.8 eV and Mo $3d_{5/2}$ at 229.7 eV from the 1H phase in the $Mo_{0.33}W_{0.67}S_2$ sample are ~ 0.3 eV lower than these binding energies of the pristine 1H MoS_2 . Mo $3d_{3/2}$ at 232.2 eV and Mo $3d_{5/2}$ at 229.1 eV from the 1T phase in $Mo_{0.33}W_{0.67}S_2$ show ~ 0.6 eV deviation from the corresponding 1H signals in the sample. Likewise, W $4f_{5/2}$ (at 35.3 eV) and W $4f_{7/2}$ (at 33.1 eV) from the 1H phase in $Mo_{0.33}W_{0.67}S_2$ are ~ 0.2 eV lower than those in the 1H WS_2 while W $4f_{5/2}$ at 34.7 eV and W $4f_{7/2}$ at 32.5 eV from the 1T phase deviate for ~ 0.6 eV from the corresponding 1H signals in $Mo_{0.33}W_{0.67}S_2$.

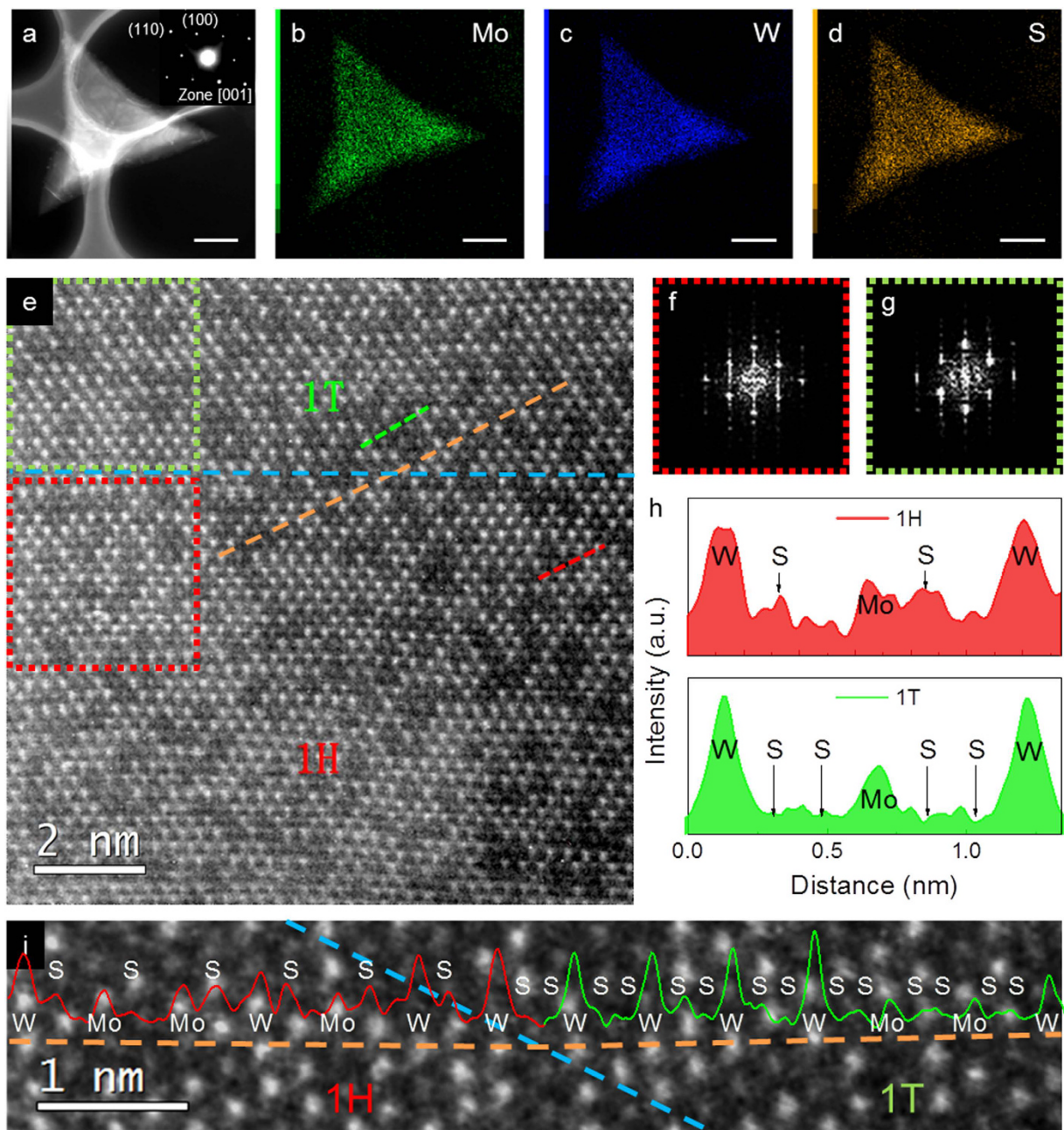


Figure 2. TEM characterization of structure and chemistry of a monolayer $\text{Mo}_{0.33}\text{W}_{0.67}\text{S}_2$ alloy. (a–d) HAADF-STEM image and EDS element mappings of Mo, W and S taken from a triangular flake. The SAED pattern (the inset of (a)) reveals the single-crystal nature of the flake. The scale bar: $1\ \mu\text{m}$. (e) High resolution HAADF-STEM image showing the atomic structure and the coexistence of 1H and 1T phases. The phase boundary is marked by a blue dashed line. (f,g) Fourier transformed images from the rectangular regions in 1T (green dot line) and 1H (red dot line) phases in (e). (h) Intensity profiles along the dashed lines in 1T and 1H regions. The upper red profile corresponds to the red dashed line in the 1H region and the lower green one is from the green dashed line in the 1T region. (i) Enlarged image of the vicinity of the orange dashed line across the phase boundary shown in (e). The intensity profile along the orange dashed line is overlaid on the image.

According to the integral intensities of Mo and W peaks from each phase, the volume ratios of 1T to 1H phases and the compositions of each phase can be approximately estimated. By plotting the volume ratio of 1T phase against the W fraction, one can see that the fraction of 1T phase shows the maximum at the composition of about the half substitution of Mo atoms (Fig. S6). In this composition range, the 2D alloys have the maximum configurational entropy and the largest lattice strain caused by the atomic size difference between W and Mo although the size difference is very small. Both the chemical effect and local lattice strains are expected to reduce the energy barrier for the phase transformation from 1H to 1T. Moreover, the thermal strains induced by the mismatch of thermal expansion coefficients between $\text{Mo}_{1-x}\text{W}_x\text{S}_2$ films and substrates may also play an important

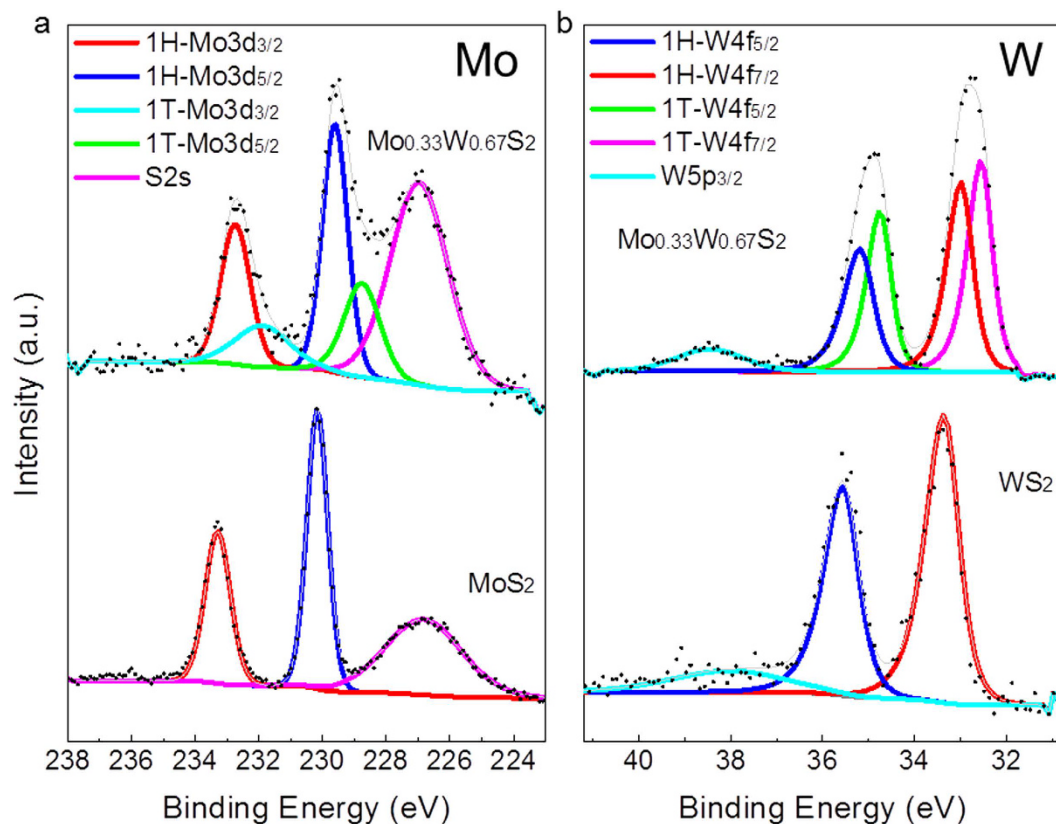


Figure 3. XPS measurements of the monolayer $\text{Mo}_{0.33}\text{W}_{0.67}\text{S}_2$ alloy, monolithic MoS_2 and WS_2 . (a) XPS spectra of Mo; and (b) XPS spectra of W. The co-existence of both 1H and 1T phase can be seen. Signals of 1H phase in $\text{Mo}_{0.33}\text{W}_{0.67}\text{S}_2$ (upper a,b) show the binding energies close to the pristine (lower a) 1H- MoS_2 and (lower b) 1H- WS_2 .

role in the formation of metastable 1T phase because the release of thermal strains by annealing can lead to the transformation from 1T to 1H. Since the 1T phase can transform into 1H phase with an unchanged Mo/W ratio by annealing at elevated temperatures, the 1H phase should be thermodynamically preferred one of the monolayer $\text{Mo}_{1-x}\text{W}_x\text{S}_2$ crystals grown by CVD, which is similar to that in the pristine MoS_2 and WS_2 ^{47,49–51,54}.

Raman and photoluminescence spectroscopy of monolayer $\text{Mo}_{1-x}\text{W}_x\text{S}_2$ crystals. Raman spectroscopy measurements were employed to characterize the structure of the monolayer $\text{Mo}_{1-x}\text{W}_x\text{S}_2$ crystals. Figure 4b shows the Raman spectra acquired at five spots along a line across a monolayer $\text{Mo}_{0.33}\text{W}_{0.67}\text{S}_2$ triangular flake on the glass substrate (Fig. 4a). The nearly identical spectra, in particular the positions of the characteristic Raman bands, further suggest the microscopic homogeneity of the as-grown 2D alloy crystals. The relatively lower intensities of the spectra from the spot 1 and 5 are because only a part of the laser beam shed on the sample at those locations. Three main phonon modes can be observed in the monolayer $\text{Mo}_{1-x}\text{W}_x\text{S}_2$ alloys under 514.5 nm excitation, assigned to WS_2 -like E' at 357.0 cm^{-1} , MoS_2 -like E' at 378.3 cm^{-1} and A'_1 at 416.5 cm^{-1} (Fig. 4b). Here, Raman modes are noted in reference to the corresponding modes in monolayer MoS_2 and WS_2 ⁵⁵. A'_1 phonon mode is the out-of-plane vibration of sulfur atoms. For MoS_2/WS_2 heterostructures, it splits into two frequencies corresponding to monolithic MoS_2 and WS_2 ⁵⁶. The observed single A'_1 mode without peak-splitting in this study provides Raman evidence that the $\text{Mo}_{1-x}\text{W}_x\text{S}_2$ alloys grown by LP-CVD are the homogeneous mixture of Mo and W atoms in solid solution, not MoS_2/WS_2 heterostructures. In addition, weak Raman signals can also be seen in the low frequency range below 250 cm^{-1} (Fig. S7, Supplementary Information), which may be the signals from the 1T phase in the 2D alloys because similar Raman bands have been observed in 1T MoS_2 and WS_2 before^{47,49,51,57}. Photoluminescence (PL) spectra from the five spots marked in Fig. 4a also show the near constant peak position of the A excitonic emission from the direct band gap at 643 nm (1.93 eV) (Fig. 4c,d), while the absence of the B excitonic emission signal, which is expected to appear at the lower wave length side of A exciton^{58,59}, suggests the high crystallinity of the 2D crystal grown by LP-CVD²¹. The nearly identical A exciton peak positions verify the homogeneous exciton energy and therefore a consistent direct band gap across the monolayer $\text{Mo}_{1-x}\text{W}_x\text{S}_2$ crystal.

Discussion

Since the composition of the $\text{Mo}_{1-x}\text{W}_x\text{S}_2$ monolayers can be customized by changing supply rates of Mo and W, $\text{Mo}_{1-x}\text{W}_x\text{S}_2$ monolayers with various Mo/W ratio (x ranging from 0–1) were grown by simply changing the amount of MoO_3 and WCl_6 precursors (Table S1, Supplementary Information). The dependence of Raman and PL spectra on Mo/W ratios of the monolayer $\text{Mo}_{1-x}\text{W}_x\text{S}_2$ alloys is shown in Fig. 4e,f. With the increase of W fraction,

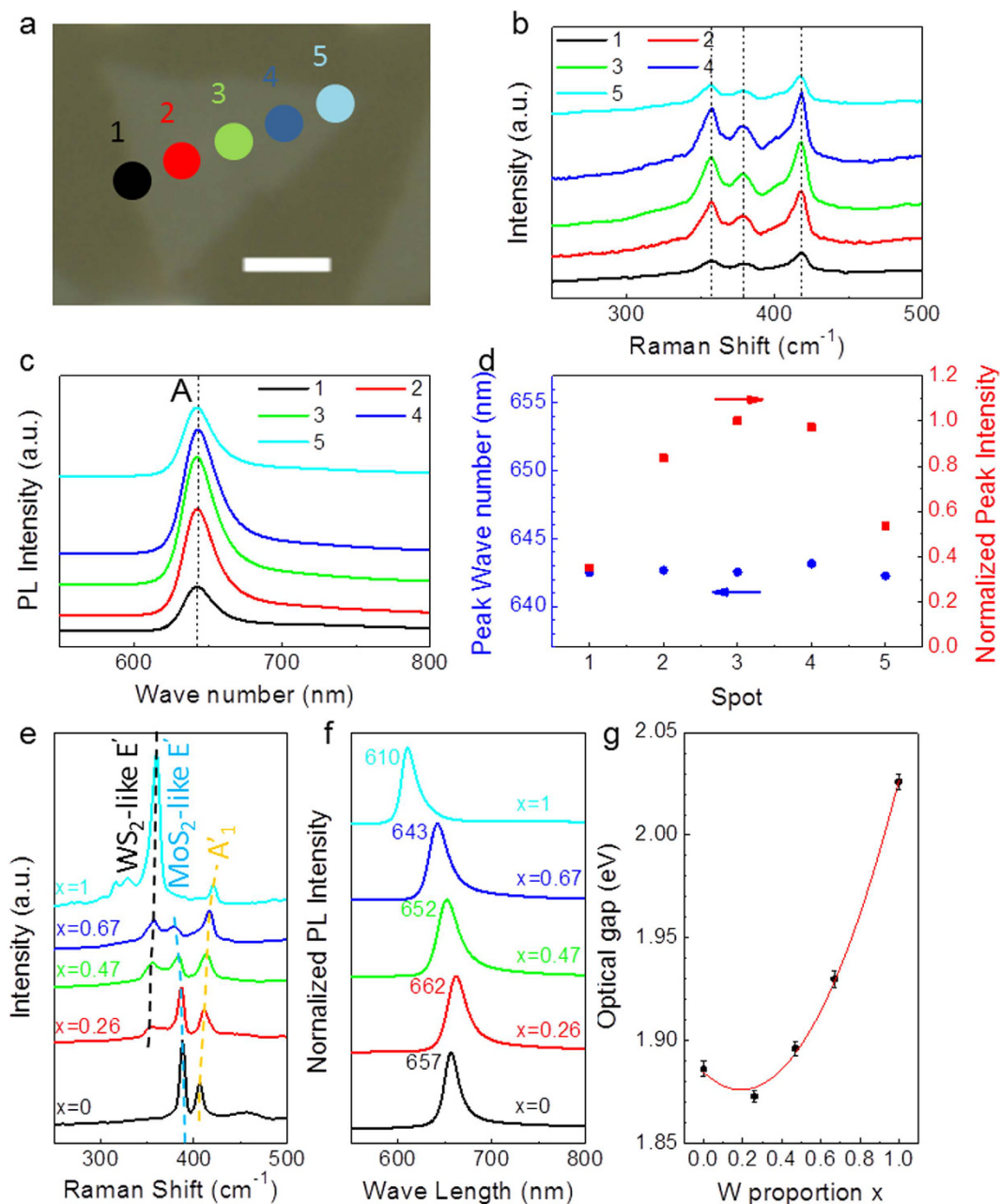


Figure 4. Raman and PL measurements of monolayer $\text{Mo}_{0.33}\text{W}_{0.67}\text{S}_2$ (for a–d) and composition dependence of Raman and PL bands of monolayer $\text{Mo}_{1-x}\text{W}_x\text{S}_2$ (for e–g). (a) Optical image of a triangular flake with marked five spots in a line cross the sample for Raman and PL measurements. Scale bar: $2\ \mu\text{m}$. (b) Raman spectra from the five spots. (c) PL spectra from the five spots. (d) Peak positions and intensities of the five PL spectra in (c). Both Raman and PL peaks show invisible changes in the positions. (e,f) The dependence of Raman and PL bands on Mo/W ratios. (g) The optical gap values as a function of W proportions in monolayer $\text{Mo}_{1-x}\text{W}_x\text{S}_2$ alloys with error bars plotted by several measurements.

WS_2 -like E' ($+2\text{LA}$) and A_1' Raman modes show blue-shift and MoS_2 -like E' shows red-shift. Meanwhile, the relative intensity of WS_2 -like E' ($+2\text{LA}$) increases and MoS_2 -like E' decreases with the increase of W. From the PL results shown in Fig. 4f,g, the optical band gaps of the monolayer $\text{Mo}_{1-x}\text{W}_x\text{S}_2$ can be calculated, which exhibits a bowing effect with the increase of Mo/W ratios. By fitting the curve with the following equation:

$$E_{\text{PL},\text{Mo}_{1-x}\text{W}_x\text{S}_2} = (1-x)E_{\text{PL},\text{MoS}_2} + xE_{\text{PL},\text{WS}_2} - bx(1-x) \quad (1)$$

the bowing factor b was calculated to be $\sim 0.26\ \text{eV}$, in good agreement with the reported value¹². Therefore, the tunable direct band gaps of the monolayer $\text{Mo}_{1-x}\text{W}_x\text{S}_2$ can be achieved by the LP-CVD method. Note that the full width at half maximum (FWHM) of the exciton peak in the PL spectra of the monolayer $\text{Mo}_{1-x}\text{W}_x\text{S}_2$ alloys

(69 meV for $x = 0.26$, 81 meV for $x = 0.47$, 80 meV for $x = 0.67$) is obviously larger than those of the pristine MoS₂ (57 meV) and WS₂ (60 meV) (Fig. 4f and Fig. S8, Supplementary Information). The enlargement of FWHM can be attributed to the large spread of band gaps under fixed x in the range of $x = 0.33 \sim 0.60$, which is the result of intrinsic polymorphism of the system predicted by a previous theoretical study⁶⁰. It is worth noting that the formation of the 1T phase does not noticeably affect the PL peak positions since the peak shift cannot be seen in the annealed samples with nearly pure 1H phase.

The successful growth of the monolayer Mo_{1-x}W_xS₂ alloys with homogeneously mixed W and Mo in 2D crystals benefits from the LP-CVD process that allows the simultaneous deposition of W and Mo at a constant atomic ratio. Moreover, the preference of hetero-atomic bonding under kinetic equilibrium conditions results in the random mixture of Mo and W atoms, which is maintained in Mo_{1-x}W_xS₂ crystals without MoS₂ and WS₂ phase separation¹³. Therefore, as long as the ratio of supply rates of Mo- and W-containing precursors is adjusted to be constant during growth, chemically homogeneous Mo_{1-x}W_xS₂ monolayers with tunable compositions and band gaps can be obtained by the LP-CVD method. After lowering down the deposition rate by reducing the amount of both precursors, growth of multilayers can be largely suppressed (Fig. S9a, Supplementary Information). And at the same time increasing deposition time leads to the coalescence of Mo_{1-x}W_xS₂ monolayer flakes into a large area sheet (Fig. S9b, Supplementary Information). Our LP-CVD method for the growth of continuous Mo_{1-x}W_xS₂ monolayer films shows notable flexibility in composition control and feasibility of mass production compared with conventional methods, such as chemical vapor transport (CVT) and mechanical/chemical exfoliation. Finally, the appearance of metastable 1T phase enables the incorporation of phase engineering into the alloying of TMDCs for device applications.

In summary, we have successfully developed a facile LP-CVD route for growing monolayer Mo_{1-x}W_xS₂ crystals using a conventional CVD system. The monolayer Mo_{1-x}W_xS₂ alloys with different compositions have intense A excitonic photoluminescence, which shows the strong dependence on Mo/W ratios of the monolayer alloys. As a result, the direct band gaps of the 2D Mo_{1-x}W_xS₂ can be continuously tuned by altering W proportions in the 2D alloys. This work may pave a new way for fulfilling the applications of band gap engineering in 2D materials by LP-CVD growth of composition-controllable monolayer alloys. In addition, the co-existence of semiconducting 1H and metallic 1T phase is for the first time observed in CVD grown 2D dichalcogenides, which may be important in tuning electronic structures and exploring superconductivity in 2D alloy crystals⁶¹⁻⁶³.

Methods

LP-CVD of monolayer Mo_{1-x}W_xS₂ alloys. Three precursor sources and a substrate were placed in the sequence of WCl₆ (Sigma Aldrich, purity 99.9%, ~5 mg), sulfur (Wako Pure Chemical Industry, purity 99%, 1.0 g), MoO₃ (Sigma Aldrich, purity >99.5%, ~5 mg) and micro slide glass substrate (Matsunami Glass, S1214) from upstream to downstream in a 2-inch quartz tube as shown in Fig. 1b. Temperatures of the sources and substrate were controlled separately by heating in different furnace zones. Ultra-pure Argon was used as the carrier gas and the pressure inside the quartz tube was controlled by adjusting the Ar flow rate. As shown in the temperature profiles in Fig. 1c, the growth recipe involves three stages: temperature rising stage (first 10 min), growth stage (next 15 min) and cooling down stage (last 5 min). In the temperature rising stage, temperatures of the sources and the substrate rose to and were stabilized at their designed values (35 °C for WCl₆, 130 °C for sulfur, 520 °C for MoO₃ and 700 °C for substrate) in 10 min under the Ar flow rate of 2000 sccm (corresponding to 5.1 mbar). In the growth stage, Ar flow rate was switched to 500 sccm (2.1 mbar) to initiate the supply of all the species to substrate for film growth. The temperatures of the precursor sources of sulfur and MoO₃ and the substrate were kept constant for 15 min while the temperature of WCl₆ gradually dropped from 35 °C to 25 °C. Finally, in the cooling down stage, WCl₆ was rapidly cooled down to 15 °C and the others to room temperature in 5 min to end the CVD growth. As-grown samples were transferred by using the standard PMMA-assisted transfer method. The as-grown samples were first spin-coated with poly(methyl methacrylate) (PMMA, Micro chem. 950K A4). 2M NaOH aq. was used to assist the detachment of samples from glass substrate. After fishing out the PMMA coated Mo_{1-x}W_xS₂ samples by other substrates, PMMA was dissolved by acetone.

Microstructure and property characterization. Raman and PL spectra were acquired by a confocal Raman spectroscopic system (Renishaw InVia RM 1000) with 514.5 nm excitation laser at the power of 10 mW and 2 mW respectively. The atomic structure and chemical analysis of the 2D alloys were characterized by HAADF-STEM and STEM-EDS by utilizing a high resolution TEM system (JEOL JEM-2100F) with double spherical aberration correctors for imaging and probing lenses. The TEM observations were performed at the acceleration voltage of 200 kV and the spatial resolution of the STEM is ~0.1 nm. XPS measurements were performed by AXIS ultra DLD (Shimadzu) with Al K α using X-ray monochromator. The peaks were fitted by Voigt functions with Lorentzian ratio of 30% and Gaussian ratio of 70% using the software CasaXPS from Casa software Ltd. The branching ratios for spin orbit split components of 3d and 4f orbitals are 3d_{5/2}:3d_{3/2} = 3:2 and 4f_{7/2}:4f_{5/2} = 4:3 respectively. Sensitive factors for Mo 3d and W 4f are 3.321 and 3.523 respectively.

References

1. Liu, Z. *et al.* Strain and structure heterogeneity in MoS₂ atomic layers grown by chemical vapour deposition. *Nat. Commun.* **5**, 5246 (2014).
2. Wang, Y. *et al.* Strain-induced direct–indirect bandgap transition and phonon modulation in monolayer WS₂. *Nano Res.* **8**, 2562–2572 (2015).
3. Conley, H. J. *et al.* Bandgap engineering of strained monolayer and bilayer MoS₂. *Nano Lett.* **13**, 3626–3630 (2013).
4. Castellanos-Gomez, A. *et al.* Local strain engineering in atomically thin MoS₂. *Nano Lett.* **13**, 5361–5366 (2013).
5. Scalise, E., Houssa, M., Pourtois, G., Afanas'ev, V. & Stesmans, A. Strain-induced semiconductor to metal transition in the two-dimensional honeycomb structure of MoS₂. *Nano Res.* **5**, 43–48 (2012).
6. Pan, J., Wang, Z., Chen, Q., Hu, J. & Wang, J. Band structure engineering of monolayer MoS₂ by surface ligand functionalization for enhanced photoelectrochemical hydrogen production activity. *Nanoscale* **6**, 13565–13571 (2014).

7. Tang, Q. & Jiang, D. Stabilization and Band-Gap Tuning of the 1T-MoS₂ Monolayer by Covalent Functionalization. *Chem. Mater.* **27**, 3743–3748 (2015).
8. Mann, J. *et al.* 2-Dimensional transition metal dichalcogenides with tunable direct band gaps: MoS₂(1-x)Se_{2x} monolayers. *Adv. Mater.* **26**, 1399–1404 (2014).
9. Su, S. H. *et al.* Band gap-tunable molybdenum sulfide selenide monolayer alloy. *Small* **10**, 2589–2594 (2014).
10. Su, S.-H. *et al.* Controllable Synthesis of Band-Gap-Tunable and Monolayer Transition-Metal Dichalcogenide Alloys. *Front. Energy Res.* **2**, 1–8 (2014).
11. Ma, Q. *et al.* Postgrowth tuning of the bandgap of single-layer molybdenum disulfide films by sulfur/selenium exchange. *ACS Nano* **8**, 4672–4677 (2014).
12. Song, J.-G. *et al.* Controllable synthesis of molybdenum tungsten disulfide alloy for vertically composition-controlled multilayer. *Nat. Commun.* **6**, 7817 (2015).
13. Wei, X.-L. *et al.* Modulating the atomic and electronic structures through alloying and heterostructure of single-layer MoS₂. *J. Mater. Chem. A* **2**, 2101–2109 (2014).
14. Li, B. *et al.* Synthesis and Transport Properties of Large-Scale Alloy Co_{0.16}Mo_{0.84}S₂ Bilayer Nanosheets. *ACS Nano* **9**, 1257–1262 (2015).
15. Chen, Y. *et al.* Tunable band gap photoluminescence from atomically thin transition-metal dichalcogenide alloys. *ACS Nano* **7**, 4610–4616 (2013).
16. Zhang, M. *et al.* Two-Dimensional Molybdenum Tungsten Diselenide Alloys: Photoluminescence, Raman Scattering, and Electrical Transport. *ACS Nano* **8**, 7130–7137 (2014).
17. Zheng, S. *et al.* Monolayers of W_xMo_{1-x}S₂ alloy heterostructure with in-plane composition variations. *Appl. Phys. Lett.* **106**, 063113 (2015).
18. Xi, J., Zhao, T., Wang, D. & Shuai, Z. Tunable electronic properties of two-dimensional transition metal dichalcogenide alloys: A first-principles prediction. *J. Phys. Chem. Lett.* **5**, 285–291 (2014).
19. Dumcenco, D. O., Kobayashi, H., Liu, Z., Huang, Y.-S. & Suenaga, K. Visualization and quantification of transition metal atomic mixing in Mo_{1-x}W_xS₂ single layers. *Nat. Commun.* **4**, 1351 (2013).
20. Lee, Y.-H. *et al.* Synthesis of large-area MoS₂ atomic layers with chemical vapor deposition. *Adv. Mater.* **24**, 2320–2325 (2012).
21. Ji, Q. *et al.* Epitaxial monolayer MoS₂ on mica with novel photoluminescence. *Nano Lett.* **13**, 3870–3877 (2013).
22. Lee, Y.-H. *et al.* Synthesis and transfer of single-layer transition metal disulfides on diverse surfaces. *Nano Lett.* **13**, 1852–1857 (2013).
23. Najmaei, S. *et al.* Vapour phase growth and grain boundary structure of molybdenum disulphide atomic layers. *Nat. Mater.* **12**, 754–759 (2013).
24. Shi, J. *et al.* Controllable Growth and Transfer of Monolayer MoS₂ on Au Foils and Its Potential Application In Hydrogen Evolution Reaction. *ACS Nano* **8**, 10196–10204 (2014).
25. Ji, Q. *et al.* Unravelling Orientation Distribution and Merging Behavior of Monolayer MoS₂ Domains on Sapphire. *Nano Lett.* **15**, 198–205 (2015).
26. Zhang, Y. *et al.* Controlled Growth of High-Quality Monolayer WS₂ Layers on Sapphire. *ACS Nano* **7**, 8963–8971 (2013).
27. Okada, M. *et al.* Direct Chemical Vapor Deposition Growth of WS₂ Atomic Layers on Hexagonal Boron Nitride. *ACS Nano* **8**, 8273–8277 (2014).
28. Rong, Y. *et al.* Controlling sulphur precursor addition for large single crystal domains of WS₂. *Nanoscale* **6**, 12096–12103 (2014).
29. Cong, C. *et al.* Synthesis and optical properties of large-area single-crystalline 2D semiconductor WS₂ monolayer from chemical vapor deposition. *Adv. Opt. Mater.* **2**, 131–136 (2014).
30. Park, J. *et al.* Layer-modulated synthesis of uniform tungsten disulfide nanosheet using gas-phase precursors. *Nanoscale* **7**, 1308–1313 (2015).
31. van der Zande, A. M. *et al.* Grains and grain boundaries in highly crystalline monolayer molybdenum disulphide. *Nat. Mater.* **12**, 554–61 (2013).
32. Ling, X. *et al.* Role of the Seeding Promoter in MoS₂ Growth by Chemical Vapor Deposition. *Nano Lett.* **14**, 464–472 (2014).
33. Fu, Q. *et al.* Controllable synthesis of high quality monolayer WS₂ on a SiO₂/Si substrate by chemical vapor deposition. *RSC Adv.* **2**, 15795–15799 (2015).
34. Xu, Z. *et al.* Synthesis and Transfer of Large-Area Monolayer WS₂ Crystals: Moving Toward the Recyclable Use of Sapphire. *ACS Nano* **9**, 6178–6187 (2015).
35. Dumcenco, D. *et al.* Large-area Epitaxial Monolayer MoS₂. *ACS Nano* **9**, 4611–4620 (2015).
36. Tan, Y. *et al.* Monolayer MoS₂ Films Supported by 3D Nanoporous Metals for High-Efficiency Electrocatalytic Hydrogen Production. *Adv. Mater.* **26**, 8023–8028 (2014).
37. Liu, H., Antwi, K. K. A., Chua, S. & Chi, D. Vapor-phase growth and characterization of Mo(1-x)W(x)S₂ (0 ≤ x ≤ 1) atomic layers on 2-inch sapphire substrates. *Nanoscale* **6**, 624–629 (2014).
38. George, A. S. *et al.* Wafer Scale Synthesis and High Resolution Structural Characterization of Atomically Thin MoS₂ Layers. *Adv. Funct. Mater.* **24**, 7461–7466 (2014).
39. Lin, Z. *et al.* Facile synthesis of MoS₂ and MoxW_{1-x}S₂ triangular monolayers. *APL Mater.* **2**, 092804 (2014).
40. Yang, Z. *et al.* Realization of high Curie temperature ferromagnetism in atomically thin MoS₂ and WS₂ nanosheets with uniform and flower-like morphology. *Nanoscale* **7**, 650–658 (2015).
41. Eda, G. *et al.* Coherent atomic and electronic heterostructures of single-layer MoS₂. *ACS Nano* **6**, 7311–7317 (2012).
42. Gao, G. *et al.* Charge Mediated Semiconducting-to-Metallic Phase Transition in Molybdenum Disulfide Monolayer and Hydrogen Evolution Reaction in New 1T' Phase. *J. Phys. Chem. C* **119**, 13124–13128 (2015).
43. Kang, Y. *et al.* Plasmonic hot electron induced structural phase transition in a MoS₂ monolayer. *Adv. Mater.* **26**, 6467–6471 (2014).
44. Duerloo, K.-A. N., Li, Y. & Reed, E. J. Structural phase transitions in two-dimensional Mo- and W-dichalcogenide monolayers. *Nat. Commun.* **5**, 4214 (2014).
45. Lin, Y., Dumcenco, D. O., Huang, Y. & Suenaga, K. Atomic mechanism of the semiconducting-to-metallic phase transition in single-layered MoS₂. *Nat. Nanotechnol.* **9**, 391–396 (2014).
46. Voiry, D. *et al.* Conducting MoS₂ nanosheets as catalysts for hydrogen evolution reaction. *Nano Lett.* **13**, 6222–6227 (2013).
47. Voiry, D. *et al.* Enhanced catalytic activity in strained chemically exfoliated WS₂ nanosheets for hydrogen evolution. *Nat. Mater.* **12**, 850–855 (2013).
48. Acerce, M., Voiry, D. & Chhowalla, M. Metallic 1T phase MoS₂ nanosheets as supercapacitor electrode materials. *Nat. Nanotechnol.* **10**, 313–318 (2015).
49. Kappera, R. *et al.* Phase-engineered low-resistance contacts for ultrathin MoS₂ transistors. *Nat. Mater.* **13**, 1128–1134 (2014).
50. Eda, G. *et al.* Photoluminescence from chemically exfoliated MoS₂. *Nano Lett.* **11**, 5111–5116 (2011).
51. Guo, Y. *et al.* Probing the Dynamics of the Metallic-to-Semiconducting Structural Phase Transformation in MoS₂ Crystals. *Nano Lett.* **15**, 5081–5088 (2015).
52. Mahler, B., Hoepfner, V., Liao, K. & Ozin, G. Colloidal Synthesis of 1T-WS₂ and 2H-WS₂ Nanosheets: Applications for Photocatalytic Hydrogen Evolution. *J. Am. Chem. Soc.* **136**, 14121–14127 (2014).
53. Chou, S. S. *et al.* Controlling the Metal to Semiconductor Transition of MoS₂ and WS₂ in Solution. *J. Am. Chem. Soc.* **137**, 1742–1745 (2015).

54. Yan, S. *et al.* Enhancement of magnetism by structural phase transition in MoS₂. *Appl. Phys. Lett.* **106**, 012408 (2015).
55. Terrones, H. *et al.* New First Order Raman-active Modes in Few Layered Transition Metal Dichalcogenides. *Sci. Rep.* **4**, 4215 (2014).
56. Gong, Y. *et al.* Vertical and in-plane heterostructures from WS₂/MoS₂ monolayers. *Nat. Mater.* **13**, 1135–1142 (2014).
57. Liu, Q. *et al.* Stable Metallic 1T-WS₂ Nanoribbons Intercalated with Ammonia Ions: The Correlation between Structure and Electrical/Optical Properties. *Adv. Mater.* **27**, 4837–4844 (2015).
58. Yu, Y. *et al.* Controlled scalable synthesis of uniform, high-quality monolayer and few-layer MoS₂ films. *Sci. Rep.* **3**, 1866 (2013).
59. Wang, X., Feng, H., Wu, Y. & Jiao, L. Controlled Synthesis of Highly Crystalline MoS₂ Flakes by Chemical Vapor Deposition. *J. Am. Chem. Soc.* **135**, 5304–5307 (2013).
60. Kutana, A., Penev, E. S. & Yakobson, B. I. Engineering electronic properties of layered transition-metal dichalcogenide compounds through alloying. *Nanoscale* **6**, 5820–5825 (2014).
61. Van Maaren, M. H., Harland, H. B. & Havinga, E. E. Critical carrier concentration for superconductivity in a CuRh₂Se₄ - based system. *Phys. Lett. A* **30**, 204–205 (1969).
62. Zakharov, O., Cohen, M. L., Louie, S. G. & Penn, D. R. Dynamical screening at the metal - semiconductor interface and excitonic superconductivity. *J. Phys. Condens. Matter* **9**, 8501–8514 (1999).
63. Ting, C. S., Talwar, D. N. & Ngai, K. L. Possible Mechanism of Superconductivity in Metal-Semiconductor Eutectic Alloys. *Phys. Rev. Lett* **45**, 1213–1216 (1980).

Acknowledgements

We thank the Institute for Material Research at Tohoku University for the assistance with the XPS measurements. We thank Prof. Takashi Goto and Prof. Hiroshi Masumoto for their valuable suggestion and discussion. This work is sponsored by JST-CREST “Phase Interface Science for Highly Efficient Energy Utilization”, JST, Japan; World Premier International (WPI) Research Center Initiative for Atoms, Molecules and Materials, MEXT, Japan, and partially supported by Japan society for the promotion of science (JSPS) Grant-in-Aid for Scientific Research on Innovative Areas “Science of Atomic Layers” (Grant No. 26107504). S. Ning is grateful for the financial support by the General Research Fund (Project number, 622813) from the Hong Kong Research Grants Council.

Author Contributions

M.C. designed the project. Z.W. conducted LP-CVD, Raman, X.P.S. and P.L. measurements. Y.I. and Y.T. contributed the LP-CVD. T.F., L.P. and A.H. performed the TEM characterization. S.N. performed the atom recognition and spatial distribution for STEM images. M.C. and Z.W. wrote the manuscript. All authors discussed the results and commented on the manuscript.

Additional Information

Supplementary information accompanies this paper at <http://www.nature.com/srep>

Competing financial interests: The authors declare no competing financial interests.

How to cite this article: Wang, Z. *et al.* Chemical Vapor Deposition of Monolayer Mo_{1-x}W_xS₂ Crystals with Tunable Band Gaps. *Sci. Rep.* **6**, 21536; doi: 10.1038/srep21536 (2016).



This work is licensed under a Creative Commons Attribution 4.0 International License. The images or other third party material in this article are included in the article’s Creative Commons license, unless indicated otherwise in the credit line; if the material is not included under the Creative Commons license, users will need to obtain permission from the license holder to reproduce the material. To view a copy of this license, visit <http://creativecommons.org/licenses/by/4.0/>